SUPPLEMENTAL MATERIAL

Australian Wildfires cause the largest stratospheric warming since Pinatubo.

Lilly Damany-Pearce et al.

S1) Qualitative assessment of the early evolution of the biomass burning aerosol (BBA) smoke plume.

In addition to its limb-sounding capabilities, OMPS on the SUOMI satellite carries a nadir mapping (OMPS-NM) spectrometer operating in the 300–380 nm wavelength range at a resolution of 1 nm (e.g. Yang et al., 2013). These wavelengths are proven in making global semi-quantitative measurements of absorbing aerosol, owing to the spectral invariance of the surface at such wavelengths and the lack of significant influence of clouds relative to absorbing aerosols on detection algorithms (e.g. Torres et al., 2007). Retrieval techniques are well proven for detection of both mineral dust and biomass burning smoke aerosols for predecessor instruments such as the Total Ozone Mapping Spectrometer (TOMS, Christopher et al., 2008) and the Ozone Mapping Instrument (OMI, Torres et al., 2007), but are only semi-quantitative owing to the dependence of the retrievals on both the absorption of the aerosol and the altitude where the aerosol resides (e.g. Christopher et al., 2011). The current OMPS-NM sensor has been used to track the evolution of stratospheric BBA plumes (e.g. Torres et al., 2020, Petersen et al., 2021, Christian et al., 2019).

The OMPS-NM retrievals do not provide aerosol optical depths, but the so-called "Aerosol Index (AI)". The AI uses two ultraviolet (UV) wavelengths and separates the impacts caused by absorbing aerosols from that of other effects, including molecular Rayleigh scattering, surface reflection, gaseous absorption and aerosol and cloud scattering (Torres et al., 1998; de Graaf et al., 2005). Figure S1 shows the evolution of the OMPS-NM AI over the first month of the event.

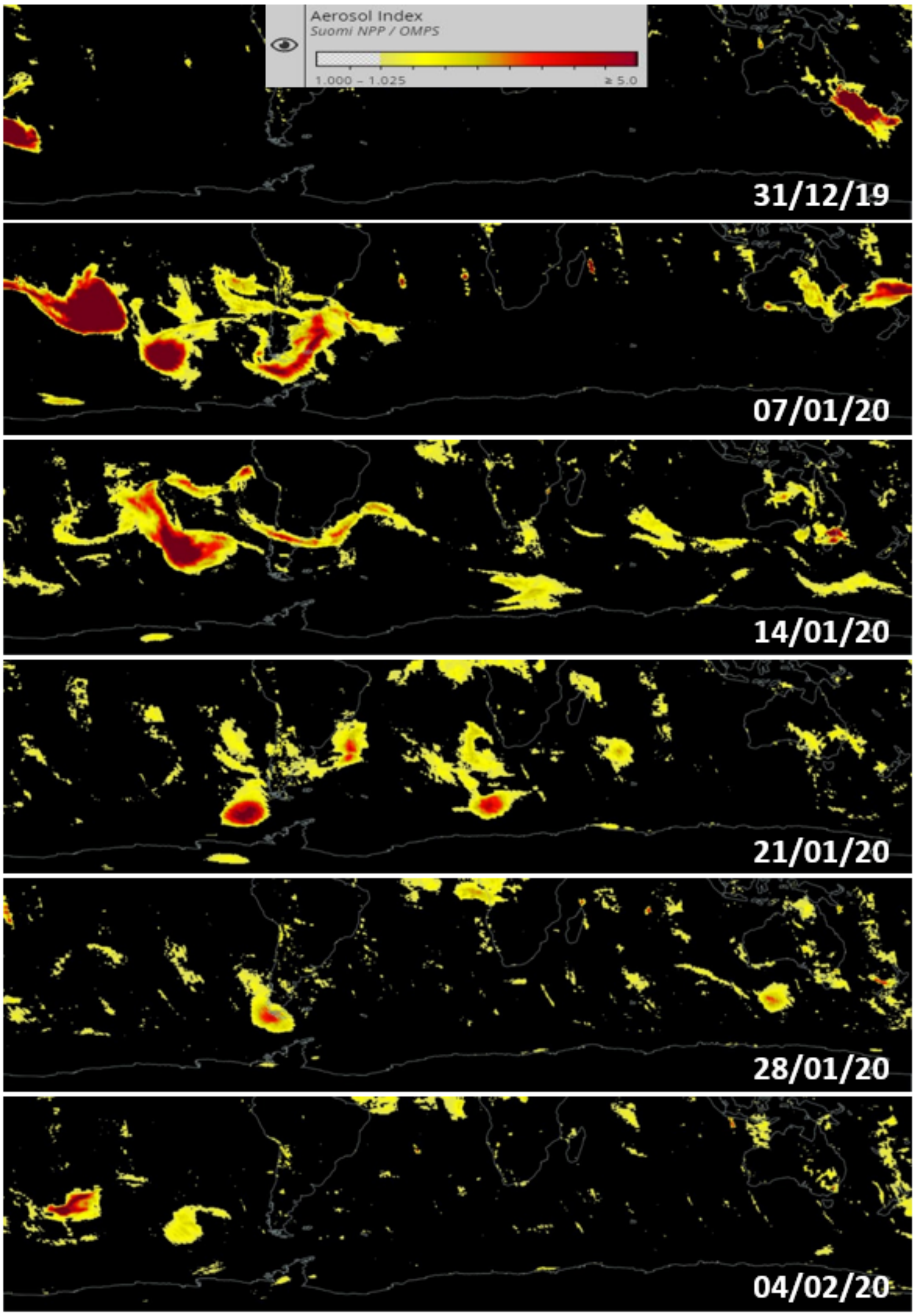

Figure S1. Showing the Aerosol Index derived from the OMPS-NM sensor on-board the SUOMI satellite over the first month of the event. The red and yellow areas show high concentrations of absorbing aerosols. Aerosol Indices of less than 1 are masked from the plots to emphasize the progression of the biomass burning smoke during the time period. Images created using NASA Worldview (https://worldview.earthdata.nasa.gov/).

S2) Diagnosing the Heating Rate caused by the BBA smoke perturbation

Before assessing the temperature perturbation caused by the BBA smoke, we assess the magnitude of the induced heating rates (Figure S2) that are provided as an output in the UKESM1 climate model. It is clear that the maximum heating rate perturbations correspond to the BBA smoke and reach a maximum in January of more than 0.2 K/day. Heating rates are generally displaced to higher altitudes than the maximum in the aerosol extinction owing to the exponential dependence of the attenuation of sunlight per unit aerosol optical depth, and also displaced to equatorial latitudes during autumn/wintertime (e.g. May/June) owing to reduced insolation at high latitudes.

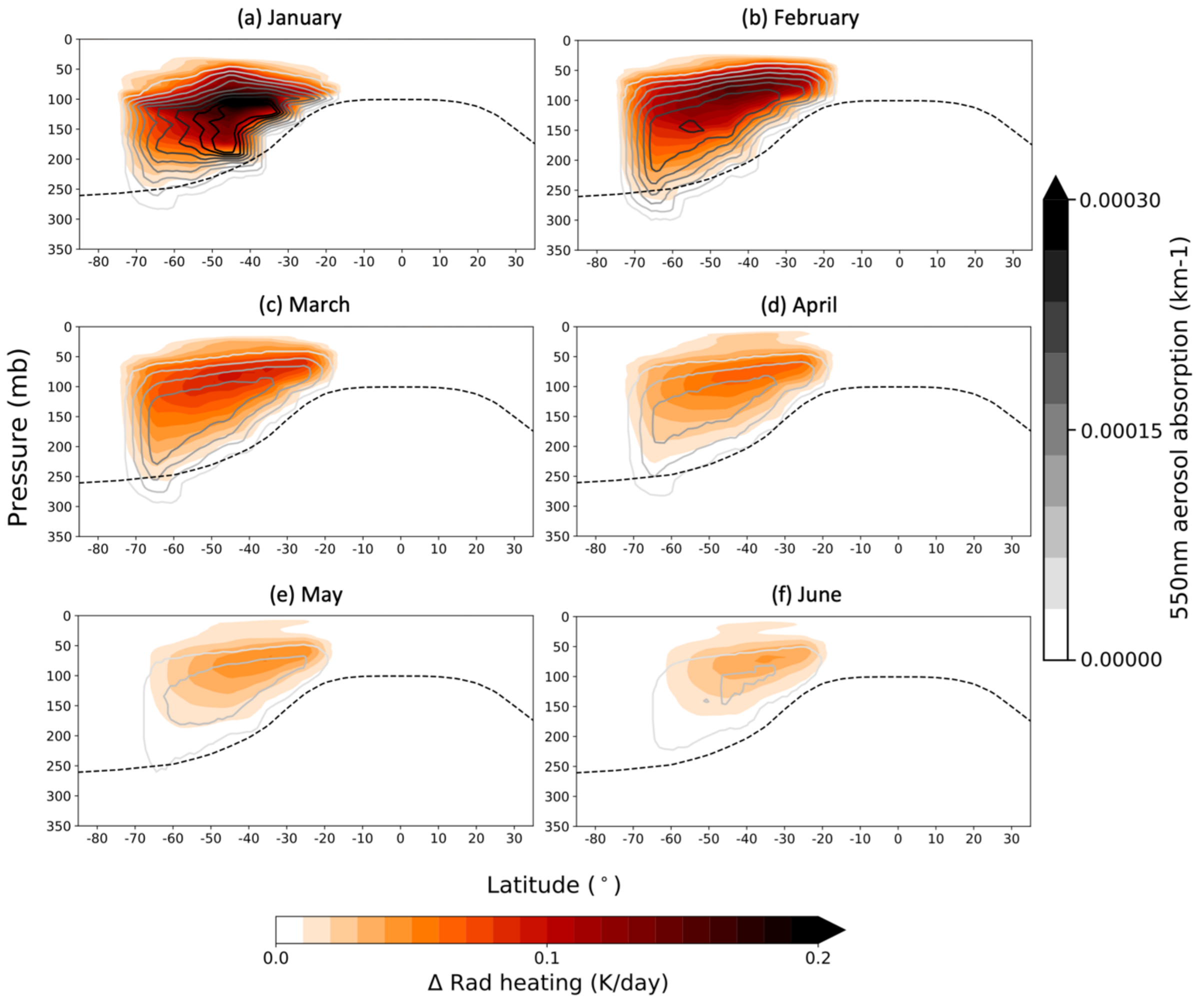

Figure S2. Monthly mean heating rate perturbation (K/day) caused by BBA smoke diagnosed over the months January-June 2019. The average monthly aerosol absorption (km^{-1}) overlaid.

S3. Assessing the relative importance of ozone in driving the LST perturbation.

Ozone is a strong absorber of solar radiation in the UV and in turn may feed back on stratospheric temperatures. The impacts on stratospheric ozone that occur from dynamical feedback processes are shown in Figure S3.

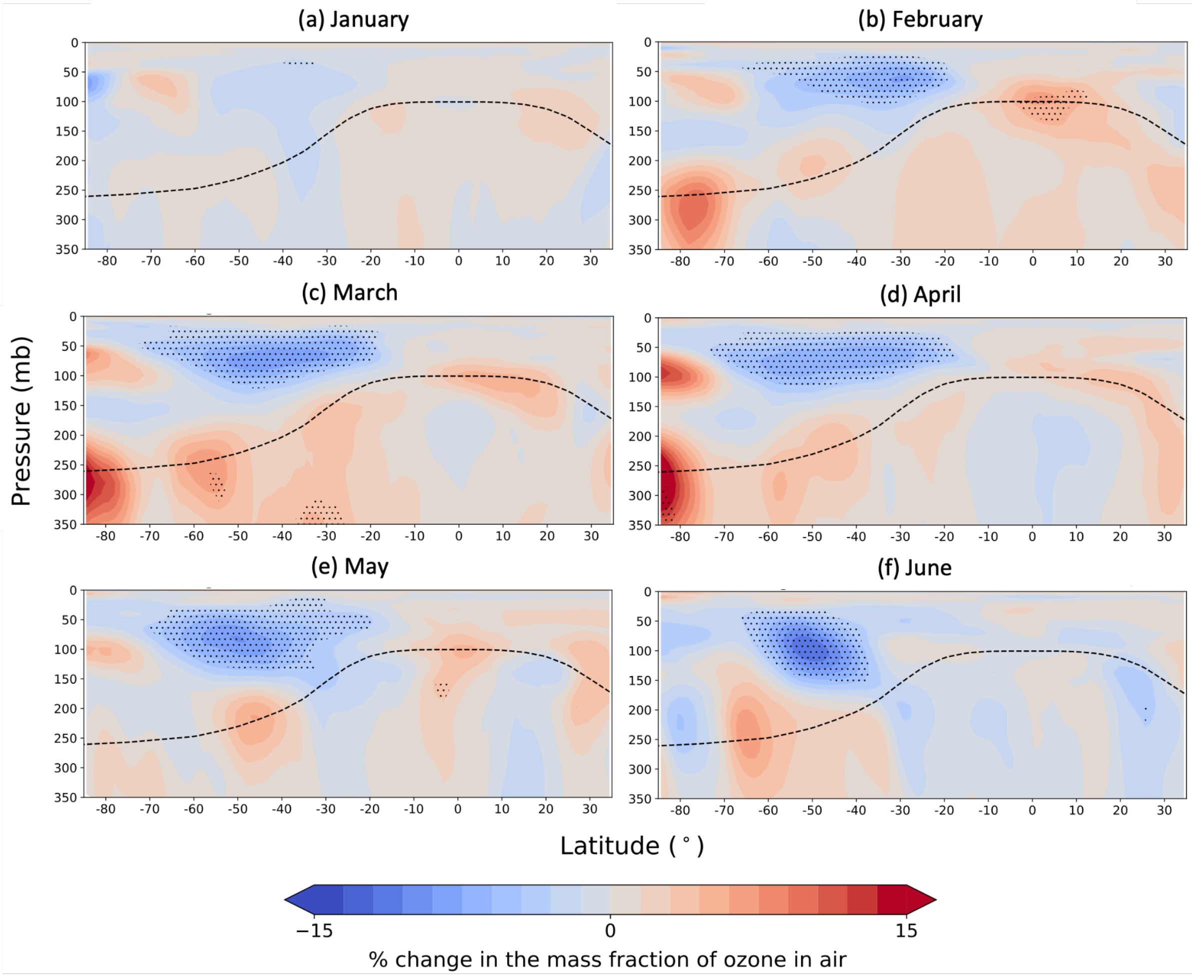

Figure S3. Monthly mean percentage change in ozone in the stratosphere and upper troposphere, due to the smoke aerosol forcing. The stippled points show the points at which the ozone amounts in the experiments were significantly different from that in the controls at a 5% significance level (calculated by Welch's t test).

Our simulations suggest that the most statistically significant (5% significance) ozone reductions occur in the stratosphere in the southern hemisphere in areas where the BBA perturbation is strongest, although there are also significant reductions in stratospheric ozone above the altitude of maximum aerosol perturbations and maximum stratospheric heating. This is consistent with other modelling results examining the impact of stratospheric sulfate aerosols (e.g. Richter et al., 2017). There are some areas where stratospheric ozone increases, but few of these reach the 5% significance level, the exception being in the UTLS over the tropics during February, which contributes to the increase in LSTs at these latitudes (Figure 3b). Similar findings have been documented in observations and modelling simulations of the impacts of stratospheric sulfate subsequent to the Pinatubo eruption (e.g. Grant et al., 1992; Telford et al., 2009), but we stress again here that our simulations do not account for heterogeneous chemistry which also has an influence on stratospheric ozone (e.g. Solomon 1999, Yu et al., 2021).

S4) Assessment of the absorption from stratospheric BBA smoke relative to sulfate aerosol

The impact of the relatively minor increase in stratospheric AOD on LSTs caused by BBA is clarified here. We derive aerosol scattering and absorption parameters (k_{sca} and k_{abs}) assuming Mie scattering theory for both sulfate and BBA smoke. For stratospheric sulfate, we assume a simple mono-modal gamma distribution as per WCP (1986). For BBA, we use a size distribution retrieved by the AERONET station at Punta Arenas (South America), averaged over the period 26 - 30th January 2020 when the stratospheric smoke layer was overhead and dominated the AOD. The refractive indices for the BBA were based on Peers et al., (2019) (see methods) and yield a single scattering albedo of 0.86 at 550nm. We calculate the optical properties across the 0.2-10μm wavelength range and weighting the derived optical properties by the incident top of the atmosphere solar flux to provide appropriate solar spectral irradiance weighted optical properties. The resulting specific scattering (k_{sca}) and specific absorption (k_{abs}) coefficients, the single scattering albedo (SSA) and the co-albedo (1-SSA) are presented in Table S1. Densities of 1.769g cm^{-3} and 1.35g cm^{-3} are assumed for sulphate and for BBA respectively.

Aerosol	k_{sca} (m^2g^{-1})	k_{abs} (m^2g^{-1})	SSA	(1-SSA)
Sulphate	3.794	0.0099	0.9974	0.0026
BBA smoke	2.764	0.4908	0.8492	0.1508

Table S1. Broadband (0.2-10.0micron) optical parameters weighted by the top of atmosphere solar spectral irradiance.

Because the size distributions are relatively similar, peaking at sub-micron wavelengths, the specific extinction (i.e. the sum of k_{sca} and k_{abs}) is relatively similar. The co-albedo provides an estimate of the absorption of the aerosols averaged over the solar spectrum. The results suggest that BBA smoke will absorb around 50 times (i.e. 0.4908/0.0099) the amount of sunlight than sulfate on an equivalent mass column loading basis.

S5) Assessment of the impact of BBA smoke on the lower stratospheric temperatures for other regions of the globe

To make a more comprehensive assessment of the impacts of the BBA smoke on the LTS, and to investigate the relative impact of the sudden stratospheric warming that occurred in September 2019 (e.g. Rao et al., 2020; Yamazaki et al., 2020), we provide analysis of observations and model simulations over the southern hemisphere (0˚-83˚S), the southern hemisphere mid-latitudes (25˚S-60˚S) and southern polar latitudes (60˚S-83˚S). These latitude bands are chosen as they are the native bands that are provided in the MSU observational records (see Methods, section M4). We also provide LST data for the northern hemisphere (0˚-83˚N).

The model simulations reveal statistically significant deviations (at a 95% confidence level, using a Student's t-test) from the mean temperature occur throughout the period February-May 2020, with the most significant perturbations occurring at mid-latitudes (25˚S-60˚S), where the modelled LST perturbations are the largest (Figure 3). The broad peak in LSTs that is modelled when BBA smoke is included also appears in the observations for both the southern hemisphere and for (25˚S-60˚S), again suggesting that BBA smoke is a primary explanatory driver.

In the model simulations at polar latitudes (60˚S-83˚S), there are no features that are significant at a 95% level although the temperature perturbation during February and March approaches this level of significance. At polar latitudes, there are several features in the observed LSTs that the model fails to capture. The sudden stratospheric warming (SSW) in September 2019 is clearly evident in the observations and is the largest on the MSU record. There is also the largest cooling on record that commences in September/October 2020, reaching its peak in November 2020. Our model simulations are free-running and cannot be expected to simulate the timing of the SSW event. In the observations, the cooling event subsequent in October and November 2020 peaks at around -9K and may be linked to maintenance of a stronger polar vortex induced by the BBA smoke, but such an inference is considered speculative at present.

In the northern hemisphere in September 2019, there is the most significant negative LST anomaly on record which more than compensates for the impact on global LSTs from the SSW event in the southern hemisphere. Whether this event occurs by chance or is related to dynamical impacts such as the role of atmospheric blocking (e.g. Shen et al., 2020) and teleconnections between the northern and southern hemisphere stratosphere (e.g. Noguchi et al., 2020) is worthy of further research.

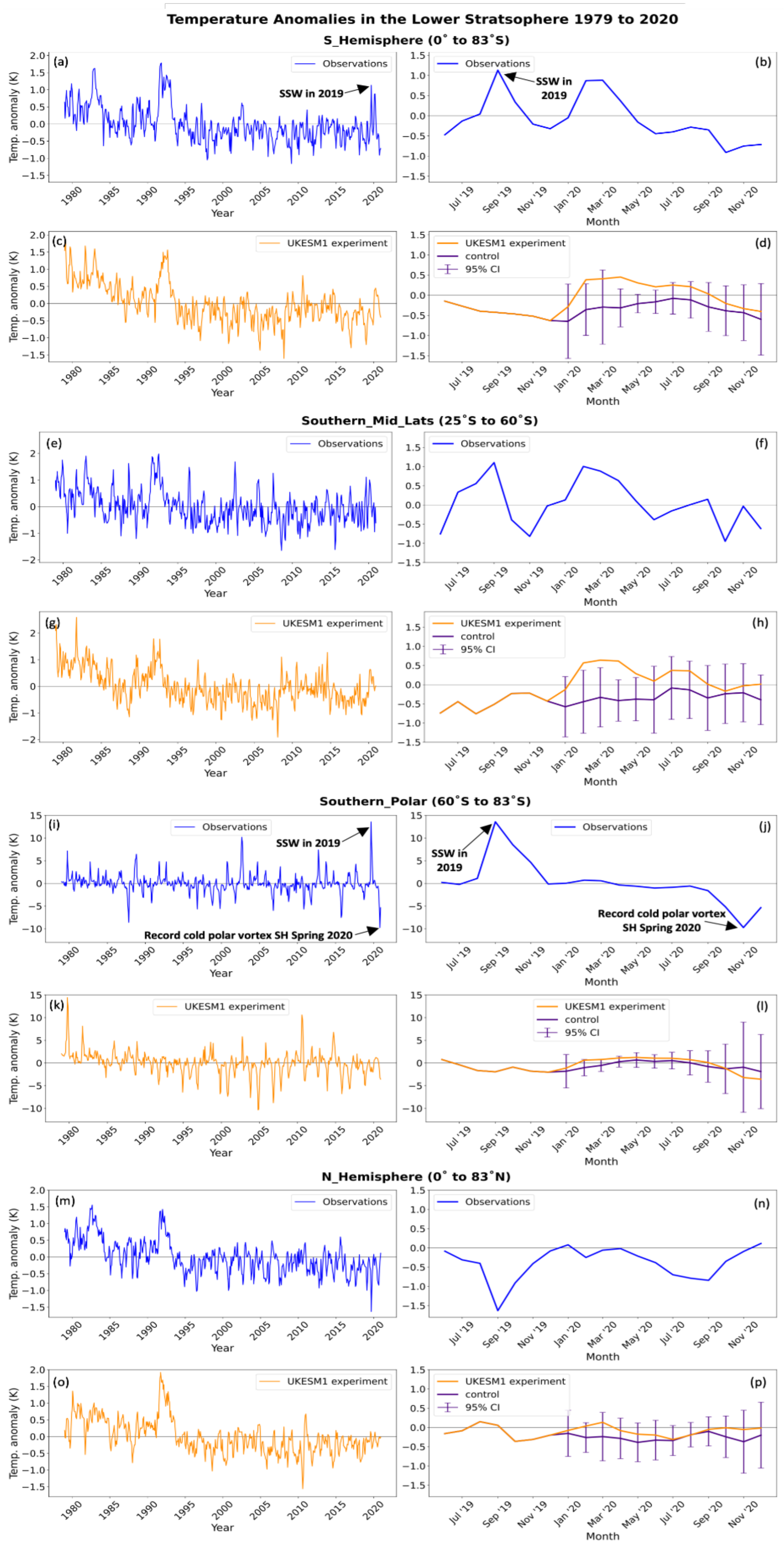

Temperature Anomalies in the Lower Stratosphere 1979 to 2020
S_Hemisphere (0˚ to 83˚S)
(a)
(b)
(c)
(d)
Observations
UKESM1 experiment
control
95% CI
SSW in 2019
Temp. anomaly (K)
Year
Month
Southern_Mid_Lats (25˚S to 60˚S)
(e)
(f)
(g)
(h)
Southern_Polar (60˚S to 83˚S)
(i)
(j)
(k)
(l)
Record cold polar vortex SH Spring 2020
N_Hemisphere (0˚ to 83˚N)
(m)
(n)
(o)
(p)

Figure S4. The monthly temperature anomalies in the lower stratosphere, from 1979 to 2020 provided by MSU/AMSU data (a,b,e,f,i,j,m,n), and the mean of 10 ensemble member UM experiment runs (c,d,g,h,k,l,o,p). Temperature anomalies are calculated from a 1979-2019 reference period, and zonally averaged for each of the latitude bands. (a-d) show the temperature anomalies over the southern hemisphere (0˚ and 83˚S), (e-h) show the temperature anomalies over the southern mid-latitudes (between 25˚S and 60˚S), (i-l) show the temperature anomalies in the southern polar region (between 60˚S and 83˚S), (m-p) show the temperature anomalies in the northern hemisphere (between 0˚ and 83˚N). (d, h, l & p) also show the temperature anomalies given by the mean of the 10 UM control runs with the 95% confidence intervals for each month of 2020, assuming a Student's t-distribution.

References: Supplementary Material

Christopher, S., P. Gupta, J.M. Haywood, G. Greed, Aerosol optical thicknesses over North Africa. Part 1: Development of a product for model validation using TOMS, MISR, and AERONET data, J. Geophys. Res., 113, D00C04, doi:10.1029/2007JD009446, 2008.

Christopher, S. A., Gupta, P., Johnson, B., Ansell, C., Brindley, H. and J.M. Haywood, (2011), Multi-sensor satellite remote sensing of dust aerosols over North Africa during GERBILS. Quart J. of the Royal Meteorological Society, 137: doi: 10.1002/qj.863, 137, 1168-1178, 2011.

De Graaf, M., Stammes, P., Torres, O. and Koelemeijer, R.B.A., 2005. Absorbing Aerosol Index: Sensitivity analysis, application to GOME and comparison with TOMS. *Journal of Geophysical Research: Atmospheres*, *110*(D1).

Grant, W.B., Fishman, J., Browell, E.V., Brackett, V.G., Nganga, D., Minga, A., Cros, B., Veiga, R.E., Butler, C.F., Fenn, M.A. and Nowicki, G.D., 1992. Observations of reduced ozone concentrations in the tropical stratosphere after the eruption of Mt. Pinatubo. *Geophysical research letters*, *19*(11), pp.1109-1112.

Noguchi, S., Kuroda, Y., Kodera, K., & Watanabe, S. (2020). Robust enhancement of tropical convective activity by the 2019 Antarctic sudden stratospheric warming. Geophysical Research Letters, 47, e2020GL088743. https://doi.org/10.1029/2020GL088743.

Shen, X., Wang, L. and Osprey, S., 2020. The Southern Hemisphere sudden stratospheric warming of September 2019. *Science Bulletin*, *65*(21), pp.1800-1802.

Solomon, S., 1999. Stratospheric ozone depletion: A review of concepts and history. *Reviews of Geophysics*, *37*(3), pp.275-316.

Telford, P., Braesicke, P., Morgenstern, O. and Pyle, J., 2009. Reassessment of causes of ozone column variability following the eruption of Mount Pinatubo using a nudged CCM. *Atmospheric Chemistry and Physics*, *9*(13), pp.4251-4260.

Torres, O., P. K. Bhartia, J. R. Herman, Z. Ahmad, and J. Gleason (1998), Derivation of aerosol properties from satellite measurements of backscattered ultraviolet radiation: Theoretical basis, J. Geophys. Res., 103(D14), 17,099–17,110.

Torres, O., Tanskanen, A., Veihelmann, B., Ahn, C., Braak, R., Bhartia, P.K., Veefkind, P. and Levelt, P., 2007. Aerosols and surface UV products from Ozone Monitoring Instrument observations: An overview. *Journal of Geophysical Research: Atmospheres*, *112*(D24).

WCP, 1986: A preliminary cloudless standard atmosphere for radiation computation. World Climate Programme Rep. WCP-112, 54 pp

Yang, K., Dickerson, R.R., Carn, S.A., Ge, C. and Wang, J., 2013. First observations of SO2 from the satellite Suomi NPP OMPS: Widespread air pollution events over China. *Geophysical Research Letters*, *40*(18), pp.4957-4962.